Confocal Bragg ptychography for bulk specimens: A numerical demonstration

Pedersen, Anders Filsøe; Chamard, Virginie; Poulsen, Henning Friis

Published in:
Optics Express

Link to article, DOI:
10.1364/OE.391282

Publication date:
2020

Document Version
Publisher's PDF, also known as Version of record

Research Article | Vol. 28, No. 11 / 25 May 2020 / Optics Express 15770
Optics EXPRESS

Confocal Bragg ptychography for bulk specimens: a numerical demonstration

ANDERS FILSØE PEDERSEN,[1,2] VIRGINIE CHAMARD,[3] AND HENNING FRIIS POULSEN[1,*]

[1]Department of Physics, Technical University of Denmark, Fysikvej 307, 2800 Kongens Lyngby, Denmark
[2]Xnovo Technology, Theilgaards Alle 9, 4600 Køge, Denmark
[3]Aix Marseille Univ, CNRS, Centrale Marseille, Institut Fresnel, Marseille, France
[*]hfpo@fysik.dtu.dk

Abstract: We report on a new X-ray imaging method, which generalizes Bragg ptychography to 3D mapping of embedded crystalline volumes within thick specimens. The sample is probed by a pencil X-ray beam. The diffracted beam is magnified by an objective and passes through a slit in the image plane to be monitored by a 2D detector in the far-field of the image plane. The dimensions of the incoming beam and the slit opening define a confocal Bragg volume. Scanning the sample with respect to this probe volume, an iterative oversampling routine is used to reconstruct the shape and projected displacement field of extended internal volumes. This routine takes into account the pupil function and known aberrations of the lens. We demonstrate the method by a numerical study of a 3.5 μm grain comprising a wall of edge dislocations. With a probe volume of ~0.12 μm^3 and a compound refractive lens with a numerical aperture of 0.49×10^{-3} as the objective, the dislocations are fully resolved with a displacement sensitivity of ~10 pm. The spatial resolution is 26×27×123 nm^3 (rms), with the poor resolution along the optical axis being limited by the probe size. With a four times larger numerical aperture, the resolution becomes 16×8×123 nm^3 (rms). The lens aberrations are found to be not critical.

1. Introduction

X-ray coherent diffraction imaging (CDI) has emerged as a powerful tool for 3D mapping of μ*m sized* isolated samples [1–5]. The method retrieves the sample scattering function from a set of coherent intensity measurements, using computational inversion approaches to determine the phase of the scattered amplitude, which cannot be directly measured by the detector. The sample image is obtained by back-propagation of the scattered field. For crystalline specimens, the intensity distribution, measured in the vicinity of a chosen Bragg peak [3–6], provides sensitivity to the crystalline properties and results in maps of the material density and of the atomic displacement projected along the Bragg vector. Spatial resolutions in the 10 nm range can be obtained with strain sensitivity in the order of a few times 10^{-4} [7]. The use of Bragg CDI (BCDI) is, until now, limited to (sub-)micrometer sized isolated crystals exhibiting rather limited strain fields. Bragg ptychography pushes the method to laterally extended crystals and larger strain fields [8–9]. Nevertheless, these approaches are still restricted to samples with a relatively limited complexity, and very often an ad-hoc sample preparation is mandatory for the success of the experiment. For studies of thick polycrystalline samples, none of these approaches are applicable, because such samples typically contain a large number of simultaneously diffracting micro- or nano-crystals within the illuminated volume. As these simultaneously diffracting crystals can likely be located far away one from the other, their individual diffraction patterns are incoherently superposed, as a result of the limited longitudinal coherence length. This makes the phase reconstruction impossible.

For 3D mapping of mm-sized polycrystalline materials X-ray imaging methods based on diffraction tomography approaches are in use: 3D X-ray diffraction (3DXRD) [10,11] and

#391282 https://doi.org/10.1364/OE.391282
Journal © 2020 Received 25 Feb 2020; revised 15 Apr 2020; accepted 15 Apr 2020; published 11 May 2020

Optics EXPRESS

diffraction contrast tomography (DCT) [12]. Space-filling 3D maps of orientations and strain tensors can be obtained for thousands of grains, however with a spatial resolution of at best 2 microns. Inserting a lens as an objective in the diffracted beam from one such grain, one may generate a magnified 3D grain map with currently 100 nm resolution [13]. In theory the latter method, known as dark field X-ray microscopy (DFXM), is compatible with a much-improved spatial resolution. In practice, it is limited in two ways. Firstly, by manufacturing errors of the lenses available leading to aberrations (thicker samples require higher X-ray energies, which so far have implied that compound refractive lenses, CRLs, were the optics of choice). Secondly, DFXM (as well as 3DXRD and DCT) although based on kinematical diffraction theory as CDI approaches, considers a measurement volume much larger than the coherence volume. Therefore, inversion of the diffraction patterns is not possible.

Recently we demonstrated a new implementation of BCDI, which is able to provide highly resolved 3D images of single interior crystals within a thick poly-crystalline sample [14,15]. The experimental set-up is a generalization of the classical BCDI configuration, where - similar to DFXM - we placed an X-ray lens in the diffracted beam from one selected interior crystal (which depending on context may be a grain or a domain). The small angular acceptance of the lens behaves as a spatial filter [14,15], which drastically reduces the diffracting volume. The 3D coherent diffraction pattern of the chosen crystal therefore is not superposed upon the diffraction patterns of other crystals. Using iterative algorithms, the shape and strain field can be reconstructed. We showed by simulations that aberrations in the objective lens has no significant effect on performance in this set up, as long as the lens is placed in the far-field of the diffracting object [14]. Next, we demonstrated the method experimentally on a 500 nm Pt grain [15]. The limitation on resolution caused by the finite numerical aperture of the objective was overcome by the Fourier synthesis of several diffraction patterns. Using a virtual image plane a spatial resolution of ~30 nm rms was obtained experimentally.

In this paper, we present a generalization of objective based Bragg CDI to a ptychographic approach, which we refer to as confocal Bragg ptychography. Conceptually it is a 3D version of the existing ptychography routines, implying that the sample is scanned in 3 non-coplanar directions and the reconstruction is based on overlap in 3D. Spurious diffraction from other elements simultaneously illuminated is completely removed in this scheme, because the scattering volume is limited by the intersection of the finite size probe and finite size lens-limited field-of-view. As a result, the intention is to apply this to study deeply embedded crystalline elements within bulk specimens. Moreover, with the limitation set by the longitudinal coherence length overcome, *the embedded grain or domain can in itself be thicker than what is allowed by classical ptychography, because the largest distance between simultaneously diffracting crystals is limited by the dimension of the probe/lens-limited intersection volume*. The requirements for the transverse coherence length are unchanged with respect to other CDI approaches. Finally, on the contrary to the forward direction geometry, for which the thin (2D) sample approximation (breaking down when thicker specimens are considered) leads to the possibility to probe a thick sample with the multi-slicing ptychography approach [16], in Bragg geometry, the sample is always considered as a 3D object. Beside the lack of coherence, the mathematical framework derived for a thin crystal is still valid for a thick crystal, preventing the use of multi-slicing inspired approaches. The paper is intended as a proof-of-concept demonstration based on numerical simulations.

The article is organized as follows: initially we present the confocal Bragg ptychography approach with a focus on a specific reconstruction algorithm. Next, we detail the numerical model used. The probe volume is chosen to be well within the capabilities of coherent diffraction imaging on small samples and the magnification is set to ~2. Simulations are performed for two configurations: one with an existing CRL as objective, and one representing the case of a four times larger numerical aperture. These simulations will be used in the third section to quantify

Optics EXPRESS

the performance of confocal Bragg ptychography, together with a detailed interpretation of the obtained results. Finally, we discuss the limitations and the potential use of this technique.

2. Confocal Bragg ptychography

2.1. Experimental

The experimental setup is shown in Fig. 1. A tightly focused pencil beam (the probe) illuminates the volume of interest inside the bulk sample. The Bragg diffracted beam is magnified and inverted by an X-ray lens leading to the definition of an image plane. The combination of the incoming beam and a 1D slit in the image plane serves to define an internal gauge volume in the sample. The detector is placed in the far-field limit as seen from the image plane. 3D mapping is achieved by scanning the position of the incoming beam in two directions in combination with scanning the slit in the image plane in one direction (or alternatively by scanning the sample in 3 directions). As with other types of ptychography, the probe footprints must strongly overlap with the neighboring probe positions (in this case in 3D) to provide redundancy in the data to allow the reconstruction to converge.

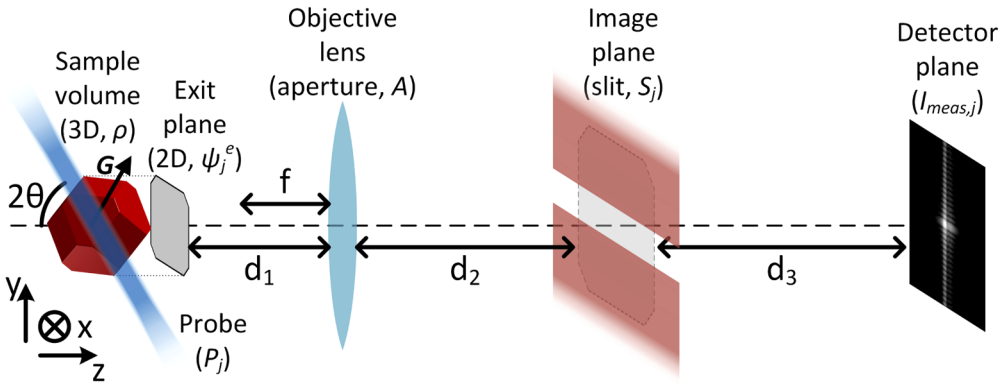

Fig. 1. Experimental setup and direct space coordinate system (x,y,z). The X-ray probe P (shown in blue) is smaller than the sample, characterized by density ρ. An objective lens placed in the diffracted beam produces a real image of the field in the exit plane of the sample, Ψ_j^e. A slit in the image plane blocks part of this beam. By translations, symbolized by subscript j, of the sample in all 3 directions (x,y,z) with respect to the probe and the slit, the entire sample is probed. The detector is placed in the far-field relative to the image plane. The distances d_1, d_2, d_3 are indicated, as is the focal length of the objective lens, f.

In terms of geometry, as illustrated in Fig. 1, the main optical axis is along the Bragg scattered beam, at an angle of 2θ to the incoming beam [17]. For all simulations, the 2θ angle will remain fixed, exactly fulfilling the Bragg condition of a chosen reflection, $\mathbf{G}_{hkl}$. The (x,y,z) orthonormal system is defined by the optical axis being the z-axis, and the yz-plane being the diffraction plane.

2.2. Reconstruction algorithm

Similar to other ptychography methods, the reconstruction algorithm for confocal Bragg ptychography is based on the overlapping approach, where the solution is obtained iteratively by imposing constraints in direct (the overlapping probe positions) and Fourier space (the intensity measurements) [18–21]. Specifically, the algorithm is heavily inspired by 3D back-projection ptychography (3DBPP) [22], which is a 3D reconstruction algorithm based on a Bragg diffraction setup with a fixed sample angle. This avoids scanning the rocking angle, thus saving time as we are already scanning the sample in 3 dimensions (x, y, and z). In our case, modeling the forward

Optics EXPRESS

and backward projections require additional steps, as the diffracted beam is manipulated by both the objective lens and the slit in the image plane.

The flow of the reconstruction algorithm is sketched in Fig. 2. The diffracted field, resulting from the intersection of the sample, ρ, and the X-ray probe P can be represented as an exit field. The algorithm can then be described in terms of the complex field ψ^s in the 4 planes: the exit plane (with superscript s = e), the objective lens plane (o), the image plane (i), and the detector plane (d). We shall assume a Fourier transform ($\mathcal{F}$, FFT) relationship between neighboring planes, implying that the objective lens is placed in the far-field of the sample – a good approximation for small sub-micron sized volumes – and that the detector is placed in the far-field relative to the image plane. Moreover, we introduce $\mathcal{R}$ as a projection operator that forms a 2D exit field from the 3D volume. The projection is along the diffracted beam direction. Let the sample density be symbolized by ρ(x,y,z), the real X-ray probe by P, the pupil function and aberrations of the objective lens collectively by the complex field A, and the attenuation of the slit in the image plane by the real field S. With these definitions, we have

$$\psi_j^d = \mathcal{F}(S_j \cdot \mathcal{F}\{A \cdot \mathcal{F}[\mathcal{R}(P_j\ \rho)]\}). \tag{1}$$

Here the subscript j labels the joint position of the probe and the slit, defining the 3D position of the illuminated volume within the sample. In the detector plane, we update the wavefront by replacing the amplitude by the measured amplitude (while keeping the phase):

$$\tilde{\psi}_j^d = \sqrt{I_{meas,j}} \cdot \frac{\psi_j^d}{|\psi_j^d|}, \tag{2}$$

where $I_{meas,j}$ is the measured intensity at sample position j. The difference between the updated and guessed wavefront is $\partial_j^d = \psi_j^d - \tilde{\psi}_j^d$.

The back-propagation from the detector plane to the sample volume becomes:

$$\partial_j^{3D} = P_j^* \cdot \mathcal{R}^\dagger(\mathcal{F}^{-1}\{A^* \cdot \mathcal{F}^{-1}[S_j \cdot \mathcal{F}^{-1}(\partial_j^d)]\}), \tag{3}$$

where * denotes the complex conjugate, and $\mathcal{R}^\dagger$ is the adjoint to the projection operator, i.e. it expands a 2D exit wave back into the 3D volume. By applying the complex conjugate of the aperture function in the back-propagation, in principle an aberration-free reconstruction is obtained, but the resolution is still affected by the pupil (numerical aperture). The final step in the algorithm for a given position j is to update the sample volume:

$$\rho = \rho - \beta \cdot \partial_j^{3D}, \tag{4}$$

where the update strength is adjusted by the β parameter, with 0< β ≤ 1. Repeating this forward- and back-projection for each probe/slit combination, j, constitutes a single cycle in the algorithm. The whole process is then repeated for k cycles, until convergence is reached. The error metric we use for monitoring convergence is:

$$Q_k = \sum_j \left(|(\psi_j^d)_k| - \sqrt{I_{meas,j}} \right)^2. \tag{5}$$

Here $(\psi_j^d)_k$ represents the field at the detector for setting j at the end of the k'th cycle.

For this proof-of-concept study we assume that the aperture function, A, (both pupil and aberrations) and slit function, S, are known *a priori*. Notably, in future the algorithm may be expanded to include optimization of both of these functions, as they remain constant for all probe/slit positions.

Optics EXPRESS

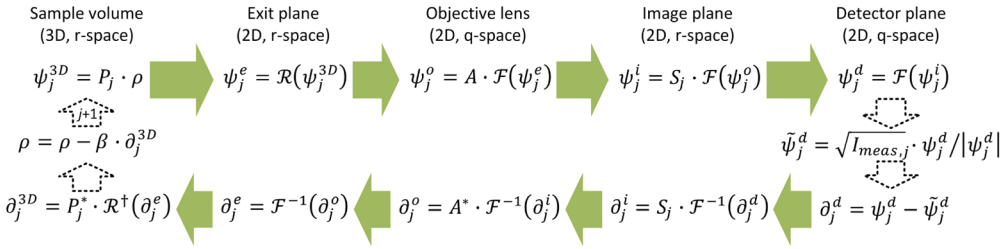

Fig. 2. A sketch of the forward- and backward-projection core of the reconstruction algorithm. The green arrows represent propagation or projection, while the equations represent the manipulations in each plane of the experimental setup.

3. Numerical model: sample design and scattered wave propagation

The proposed methodology is tested through numerical simulations. Following usual practice for dark field microscopy with hard X-rays [13,23], the objective is a CRL [24]. Initially we assume that the incoming beam is fully coherent, both transversally and longitudinally, with respect to the dimension of the diffracting volume.

3.1. Sample model

The sample is an Al grain with the shape of a truncated octahedron (see Fig. 1). The grain diameter is 3.5 µm. To model the grain scattering function, we used the same approximation as in Bragg CDI: the scattering function from the sample is complex; the amplitude represents the electron density and the phase $\varphi(\mathbf{r})$ is the displacement field $\mathbf{u}(\mathbf{r})$ projected onto the diffraction vector $\mathbf{G}_{hkl}$, $\varphi(\mathbf{r}) = \mathbf{u}(\mathbf{r}) \cdot \mathbf{G}_{hkl}(\mathbf{r})$. Here the electron density is assumed to be constant inside the grain (homogeneous material), while the phase represents the displacement field from a dislocation wall comprising identical edge dislocations. The dislocation lines are parallel and aligned with the z-axis, with the dislocation wall in the yz-plane (see Fig. 3).

3.2. Generation of phantom data

We use a fractional Fourier transform (FrFT) approach [25,26] to generate the diffraction data. We have previously demonstrated that this approach accurately and efficiently takes into account the thick-lens behavior of a CRL objective lens and its use for both dark field microscopy and Bragg CDI [14]. For each position of the probe (P_j) the exit field is calculated as a sum (projection) of $P_j \cdot \rho$ along the exit direction, the z-axis. The exit field is forward-propagated to the exit plane of the CRL by a single FrFT transform, at which point the aperture is applied (taking into account both the pupil and aberrations, while ignoring the vignetting of the CRL, as the field-of-view is much larger than the object). Another FrFT transform propagates the resulting field to the image plane. Here the filtering of the slit is modelled by a simple binary function. Finally, the field is propagated by yet another FrFT to the detector, where the intensity is calculated from the electric field amplitude, $I(\mathbf{q}) = |E(\mathbf{q})|^2$. The aberrations are modelled from measured aberrations of a CRL [27].

3.3. Parameters used in simulations

The X-ray beam energy is 17 keV ($\lambda = 0.73$ Å), the chosen reflection (333), and the Bragg angle consequently $\theta = 28°$. The sample volume consists of 256×256×256 voxels in total spanning 5 µm in all three directions - so the voxel size is 19.5^3 nm^3. The phase of the object is inspired by the displacement field from 17 edge dislocations in the zy-plane - evenly spaced by a distance of 208 nm. Only one component of the displacement field was used.

Optics EXPRESS

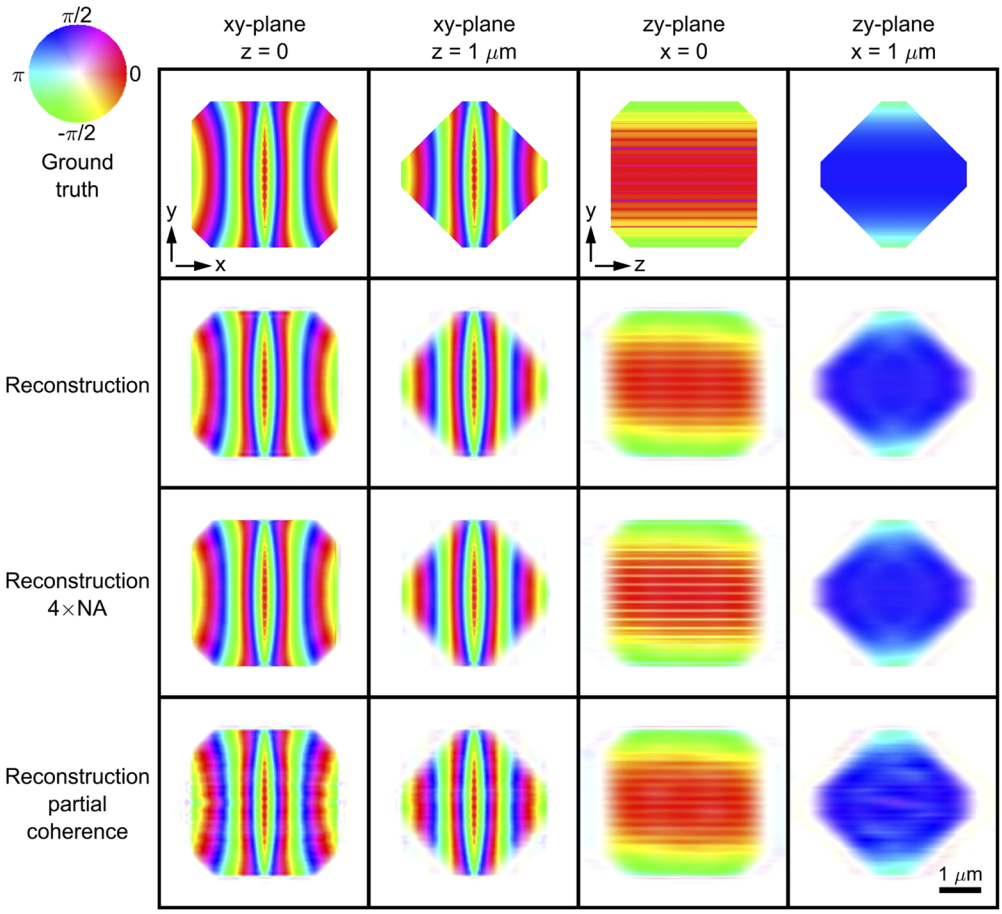

Fig. 3. Ground truth and reconstructions for the simulations with a typical CRL (second row) as objective, with an objective with a 4 times larger NA (third row), and with a conventional CRL and finite longitudinal coherence (bottom row). The sample comprises 17 parallel and straight edge dislocations placed in the *zy* plane. Four cuts through the sample are shown: center and off-center cuts in the *xy*-plane perpendicular to the optical axis and center and off-center cuts in the scattering plane (*zy*-plane).

Optics EXPRESS

The first numerical experiment was performed with a Be CRL as objective with $N = 70$ identical lenslets with an apex radius of curvature of $R = 50$ μm, and thickness $T = 1.6$ mm, giving an effective focal length of $f = 26.5$ cm [17]. The sample-lens distance is $d_1 = 42.0$ cm, which forms an $M = 2.08$ times magnified real image $d_2 = 93.5$ cm from the lens exit. In this configuration, the RMS width of the Gaussian acceptance angle is $\sigma_a = 209$ μrad [17], corresponding to a numerical aperture (FWHM) of 0.491×10^{-3}. The detector is placed $d_3 = 3.00$ m from the image plane and has a pixel size of 21 μm.

In a second numerical experiment, we artificially increased the numerical aperture by a factor of 4, while keeping the remaining parameters of the set-up constant. This experiment does not represent a realistic CRL but provides an estimate of the effect of introducing new lens technologies (e.g. multi-layer Laue lenses [28]) with an increased numerical aperture. This allows us to explore the impact of the limited aperture on the reconstruction quality.

The incoming beam is for both experiments a real Gaussian with an RMS width of $w_p = 195$ nm. The coordinate system is centered on the object. The beam is scanned in a square grid perpendicular to the beam direction. The step size is 263 nm, which gives an overlap of 64% between neighboring positions. The slit function is a square function, which is 1 inside the slit opening and 0 outside. The slit width is $w_s = 1.3$ μm, corresponding to 625 nm in the sample plane (due to the magnification). The slit is translated perpendicularly to the slit opening in steps of 866 nm (effectively 417 nm in the sample plane). This leads to a total probe volume of 0.124 μm^3 (given by the FWHM of the beam and the projected slit size). In order to cover the entire sample volume with this probe/slit size, 1800-1900 probe positions were used per reconstruction (the probe/slit positions with images containing less than 1 ‰ of the intensity of the most intense probe position were discarded).

The intensity at the detector is subject to photon shot-noise, and so the intensity at each pixel (for each probe position) is discretized using a Poisson distribution of noise. Before discretization, the intensity is scaled such that the most intense pixel has an expectation value of 1,000,000 photons. This is set quite high to highlight the limitations of the reconstruction method itself rather than the effect of noise. However, with future X-ray sources this signal is seen as achievable.

In a final experiment we include the effects of limited longitudinal coherence by introducing a finite energy bandwidth of the source. The geometry of the set-up is not changed. In confocal Bragg ptychography the optical path length difference is given as $OPLD = (w_p + w_s/M) \cdot \tan\theta$. The OPLD is calculated by assuming parallel rays entering along the probe direction, separated by a maximum distance of the probe size (w_p). The rays exit the sample at an angle of 2θ, separated by a maximum of the projected slit size (w_s/M). Using the parameters above (with FWHM beam width) OPLD = 575 nm. To have a longitudinal coherence length (ξ_l) exceeding the OPLD we choose a source bandwidth (FWHM) of $\Delta E/E = 0.5\times10^{-4}$, giving $\xi_l = 729$ nm at this energy. For this simulation we performed a fully coherent simulation as described above at 31 distinct energies in the range $E \pm 2\Delta E$. The detector signal is found as the sum of the intensity from each energy weighted by a Gaussian with a FWHM of ΔE.

In all cases the feedback parameter is initially set to $\beta = 0.9$, then gradually decreased to $\beta = 0.8$ to optimize convergence. The initial guess is that the volume to be reconstructed is empty, hence no prior information on the shape of the sample is used. In total $k = 100$ cycles are performed for each reconstruction. The error metric shows fast monotonic convergence.

4. Resulting reconstructions

The results for the three simulations are shown in Fig. 3 along with the ground truth (the phantom). The figure shows four planes through the sample, representing center and off-center positions in both the *xy*-plane (perpendicular to the optical axis) and the *zy*-plane (in the scattering plane).

Initially we report on the reconstructions of the two simulations with full longitudinal coherence, shown in the second and third row in Fig. 4. Here we found that the phase deviated from the

Optics EXPRESS

ground truth by a parabola in the *xy*-plane. The origin of this was found to be that the detector is not sufficiently far away to be in the ideal far-field limit. This fact is captured by the FrFT propagation, but not in the reconstruction algorithm utilizing regular FFTs. (The angle in the FrFT is 0.495π instead of $\pi/2$, corresponding to a Fresnel number of 7.53×10^{-6}.) By propagating a real-valued object (with no phase), we made a calibration for this spherical phase factor. The reconstructions shown in Fig. 3 represent results after applying this calibration. (In typical ptychography experiments where the coordinate system is centered on the probe this phase parabola appears on the probe rather than the object and can easily be taken into account [29].)

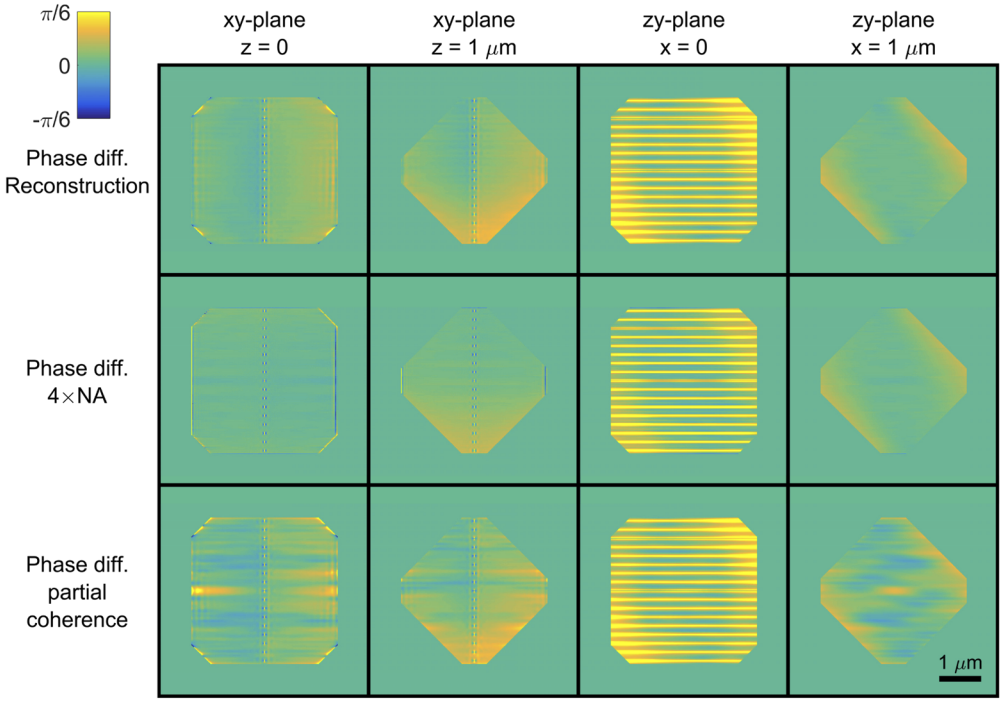

Fig. 4. Phase difference between the different reconstructions and the ground truth. The 4 planes through the sample object are the same as in Fig. 3. The phase at the center of the dislocations are different from the ground truth, but otherwise the agreement is very good. Notice the limited range of the color scale.

The reconstructions show very good agreement with the ground truth, and the individual dislocations in the dislocation wall are clearly resolved. This is also seen in the phase difference map shown in Fig. 4. To evaluate the spatial resolution, we plot the average amplitude in Fourier space of the ground truth and the two reconstructions in the x, y and z direction, see Fig. 5. We fit a modulation transfer function (MTF) model - the ground truth Fourier amplitude multiplied by a Gaussian MTF - to the reconstruction Fourier amplitudes. The resulting fit can be used to estimate the RMS resolution. For the typical CRL case we estimate the RMS resolution to be $26\times27\times123$ nm^3, and for the 4× NA case it is $16\times8\times123$ nm^3. The *xy*-resolution figures should be compared to an expected RMS resolution (as estimated by 0.61 λ/NA/2.35) of 39 nm for the typical CRL and 23 nm for the improved lens.

This set of results motivates several comments, listed below:

- The results are not impacted by the *lens aberrations*, provided these are known. Also, at first sight it may be surprising that a Fourier transform between exit plane and objective lens plane is permissible, as the true Fourier plane is the back focal plane. However, the working

Optics EXPRESS

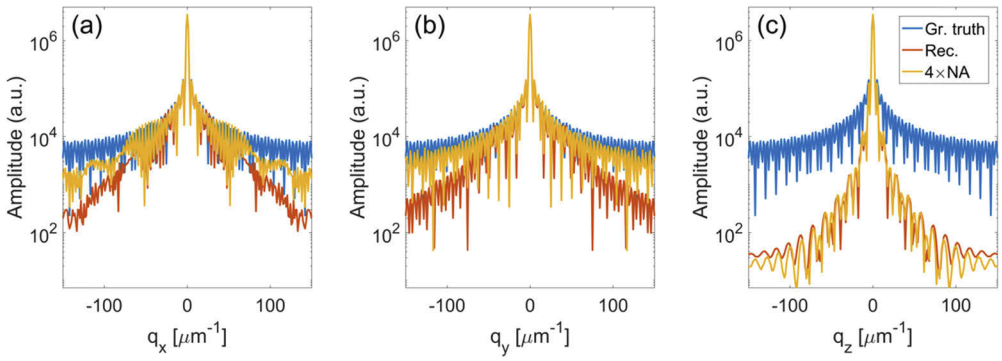

Fig. 5. Modulation transfer function (MTF) in the (a) x-direction, (b) y-direction, and (c) z-direction for the ground truth and the two reconstructions, cf. Figure 3.

distance from exit plane to entry of the lens is sufficiently long for the CRL entry point to be effectively in the far-field limit (the Fractional Fourier angle is 0.499π, corresponding to a Fresnel number of 9.83×10^{-6}). Similar observations were made in our previous work on objective based BCDI [14,15].

- Hence, the objective only limits the resolution by the finite *numerical aperture*.

- There is an *anisotropy* in the resolution for the 4×NA case. We believe this reflects that the resolution is limited by noise in this case. When limited by noise the scanning of the slit in the y-direction provides additional information to the reconstruction, giving a better resolution in the y-direction than in the x-direction.

- The resolution in the z-direction is significantly lower than in the other directions, and is independent of the NA, as expected. We attribute this to the resolution being determined by the *beam size*, which follows from the reconstruction algorithm. The localization in the z-direction is given by $\partial_j^{3D} = P_j^* \cdot \mathcal{R}^\dagger(\partial_j^e)$; the multiplication by P defines the resolution in the z-direction.

Finally, the simulation with partial coherence resulted in a successful reconstruction - shown in Fig. 3, bottom row - with a longitudinal coherence length significantly smaller than the OPLD for a typical Bragg ptychography setup (or BCDI setup). These results highlight the strength of this technique, as it overcomes sample size limitations in all 3 spatial directions.

5. Discussion and conclusion

The above results document the potential of confocal Bragg ptychography: the scattering arising from different parts of the crystal can be separated in the measured signal. The superior features of X-ray Bragg coherent diffraction imaging/ptychography is extended to observations of micron-sized objects inside bulk specimens. The methodology presented may also be used for mapping a region within larger crystals/grains/domains.

This work extends the previous work on objective based Bragg CDI [14,15]. In both cases, the numerical aperture is found from simulations to be the limiting factor for spatial resolution. The set-up for objective based Bragg CDI is arguably simpler and one can improve the resolution by introducing a virtual image, which is not possible with confocal Bragg ptychography. As already mentioned, a main advantage of confocal Bragg ptychography is that it extends the use of coherent methods to deeply embedded diffraction units (grains or domains) with dimensions larger than the lateral coherence length. Moreover, heuristically it has been found that a mapping

Optics EXPRESS

with Bragg ptychography can be performed with about 1% of the photons required for a Bragg CDI map with the same resolution, due to the better sampling obtained from constraints in direct space. We foresee that the same advantage will be associated with confocal Bragg ptychography (in the (*xy*-plane) in comparison to objective based Bragg CDI.

The slit has been idealized to be a 0/1 function in the presentation above. We expect that the practical implementation will require a detailed characterization of the slit function. As long as the slits are sharp enough to produce some structures in the associated Fourier space, the slit profile shall not be detrimental to the ptychography approach, which is known to take advantage of all kinds of spatial diversities. Along the same line, the beam has been designed as a real Gaussian, i.e. with flat wave-front at the focal plane. While this is an approximation of a realistic beam, we anticipate that any curvature will improve the sensitivity with respect to strain distribution and lattice rotation, at least for weakly in-homogeneously strained materials. However, this improvement would likely be marginal once compared to strain and lattice rotation expected in realistic materials.

In the following we discuss the quality of the reconstructions performed in more detail, address general limitations of the technique and comment on future applications.

5.1. Quality of reconstruction

The algorithm presented is a generalization of a known ptychography algorithm [22]. While the results are very encouraging, other reconstruction approaches may be relevant. In particular, with methods based on acquisition of a rocking curve, we expect to obtain an isotropic resolution, in addition to the possibility to gain sensitivity to other strained and misoriented crystalline parts in the probed volume. These later ones would mostly appear as missing volume in the single angle approach.

The phase sensitivity, which can be evaluated by the amplitude of the phase fluctuations exhibited in our reconstructions, corresponds to a displacement on the order of 10 pm. This agrees with the usual performances of classical Bragg CDI.

The approach introduces several new degrees of freedom such as the magnification – which couples to slit opening - the dimensions of the X-ray probe as well as the spatial overlap. In the example, we chose what we consider to be realistic parameters. An optimization of these with respect to time and space resolution, 3D volume mapped, error-robustness and contrast will be sample specific as well as specific to the size of the laboratory and the lenses available and is outside the scope of this presentation.

5.2. Limitations of the method

- The finite *numerical aperture* of the CRL is an obvious limitation. This work is motivated in part by recent progress on wedged Multilayer Laue Lenses, MLLs. For these lenses, a spot size of 8 nm was demonstrated at 8 keV in [30] with a pair of lenses exhibiting a numerical aperture of 2 mrad (FWHM) and a high reflectivity. For wedged MLLs the focal length and numerical aperture may be chosen freely in principle, but the physical aperture is limited to about 100 µm [31,32]. Recently, we have experimentally demonstrated the use of such lenses as objectives for hard X-ray microscopy [28]. NAs of 4×10^{-3} seem within reach, which is 10 times the value used for the "typical CRL" case above. At the same time, powerful methods for characterizing the aberrations in the exit plane of the lens - such as speckle tracking - are maturing. At the expense of increasing data acquisition time another potential approach to overcome the limitation is to use Fourier synthesis, i.e. scanning the numerical aperture in reciprocal space to acquire several 3D diffraction patterns, all of them being simultaneously used in the inversion process to enlarge the effective numerical aperture [15,33].

Optics EXPRESS

- The *photon statistics* is quite favorable in the simulated cases. Interestingly, reducing the number of photons will only serve to decrease the difference between coherence-based mapping using configurations with and without the use of lenses, as the photon statistics will become the dominant source of errors.

- Bragg CDI methods are well known to be limited in terms of handling inhomogeneous *strain*. As the reconstruction principle applied here is a generalization of such methods, we do not anticipate restrictions for strain characterization beyond those applying to the existing Bragg ptychography algorithms., which has been shown to be quite robust to non-homogeneous strain fields [34]. More sophisticated Bragg CDI and ptychography algorithms taking into account e.g. 2D probe reconstruction may also be generalized to confocal Bragg ptychography.

- The phantom used in the simulations has less structure in the z-direction, which has the lowest resolution. More realistic phantoms should be used for further work. If the phase features in the z-direction prove more challenging to reconstruct, one may include measurements at a few different rocking angles, as discussed above.

- The results shown are based on the pre-knowledge of all experimental parameters, including probe profile, aperture, slits, positions etc. Several works have already demonstrated the ability of ptychography approaches to retrieve more than just the sample scattering function, thanks to the large amount of information in the data set [19]. We expect similar improvements are possible with the confocal Bragg ptychography method.

5.3. Further perspectives

Some aspects of confocal Bragg ptychography can only be addressed experimentally. This includes the potential effect of other parts on the sample on the wavefronts. The actual *implementation* at a synchrotron beamline will require a dedicated set-up, due to the challenging specifications with respect to simultaneous alignment of probe, sample, objective and slit.

The X-ray microscopy set-up presented can be exploited in other ways. As an example, at the beamline ID06 at ESRF a high resolution 2D detector can be installed in the image plane, to be exchanged with the slit by means of a translation stage [35]. We foresee that it might be interesting to investigate reconstructions based on combined measurements in the image plane and the confocal Bragg ptychography approach presented above, specifically for samples presenting non-homogenous strain fields. The combined information arising from two conjugated spaces should lead to an improvement of the robustness with respect to strain field imaging. This will require an optimized reconstruction algorithm.

Experimental demonstrations are under development. Notably, confocal Bragg ptychography can be implemented at existing synchrotron setups. One option is to use a beamline optimized for classical Bragg CDI or ptychography and add the objective and slit. Another option is to use an existing DFXM beamline and collimate the incoming beam sufficiently to make a coherent volume fraction matching the requirements of classical Bragg CDI.

Funding

European Research Council (291321); H2020 European Research Council (724881); Danish Agency for Science and Higher Education (4059-00009B).

Acknowledgments

The authors would like to thank C. Detlefs, M. Allain and P. Li for fruitful discussions.

Optics EXPRESS

Disclosures

The authors declare no conflicts of interest.

References

1. D. Sayre, "Some implications of a theorem due to Shannon," Acta Crystallogr. **5**(6), 843 (1952).
2. J. Miao, P. Charalambous, J. Kirz, and D. Sayre, "Extending the methodology of X-ray crystallography to allow imaging of micrometre-sized non-crystalline specimens," Nature **400**(6742), 342–344 (1999).
3. H. Chapman and K. Nugent, "Coherent lensless X-ray imaging," Nat. Photonics **4**(12), 833–839 (2010).
4. J. Miao, T. Ishikawa, I. K. Robinson, and M. M. Murnane, "Beyond crystallography: Diffractive imaging using coherent x-ray light sources," Science **348**(6234), 530–535 (2015).
5. M. A. Pfeifer, G. J. Williams, I. A. Vartanyants, R. Harder, and I. K. Robinson, "Three-dimensional mapping of a deformation field inside a nanocrystal," Nature **442**(7098), 63–66 (2006).
6. A. Yau, W. Cha, M. W. Kanan, G. B. Stephenson, and A. Ulvestad, "Bragg coherent diffractive imaging of single-grain defect dynamics in polycrystalline films," Science **356**(6339), 739–742 (2017).
7. V. Chamard, M. Allain, P. Godard, A. Talneau, G. Patriarche, and M. Burghammer, "Strain in a silicon-on-insulator nanostructure revealed by 3D x-ray Bragg ptychography," Sci. Rep. **5**(1), 9827 (2015).
8. V. Chamard, J. Stangl, G. Carbone, A. Diaz, G. Chen, C. Alfonso, C. Mocuta, and T. H. Metzger, "Three-Dimensional X-Ray Fourier Transform Holography: The Bragg Case," Phys. Rev. Lett. **104**(16), 165501 (2010).
9. F. Mastropietro, P. Godard, M. Burghammer, C. Chevallard, J. Daillant, J. Duboisset, M. Allain, P. Guenoun, J. Nouet, and V. Chamard, "Revealing crystalline domains in a mollusc shell single-crystalline prism," Nat. Mater. **16**(9), 946–952 (2017).
10. H. F. Poulsen, *Three-Dimensional X-Ray Diffraction Microscopy* (Springer, 2004).
11. H. F. Poulsen, "An introduction to three-dimensional X-ray diffraction microscopy," J. Appl. Crystallogr. **45**(6), 1084–1097 (2012).
12. W. Ludwig, S. Schmidt, E. M. Lauridsen, and H. F. Poulsen, "X-ray diffraction contrast tomography: a novel technique for three-dimensional grain mapping of polycrystals. I. Direct beam case," J. Appl. Crystallogr. **41**(2), 302–309 (2008).
13. H. Simons, A. King, W. Ludwig, C. Detlefs, W. Pantleon, S. Schmidt, F. Stöhr, I. Snigireva, A. Snigirev, and H. F. Poulsen, "Dark-field X-ray microscopy for multiscale structural characterization," Nat. Commun. **6**(1), 6098 (2015).
14. A. F. Pedersen, V. Chamard, and H. F. Poulsen, "A numerical study of Bragg CDI on thick polycrystalline specimens," Opt. Express **26**(18), 23411 (2018).
15. A. F. Pedersen, T. Zhou, C. Detlefs, G. Carbone, V. Chamard, and H. F. Poulsen, "X-ray coherent diffraction imaging with an objective lens: towards 3D mapping of thick polycrystals", Phys. Rev. Research (to be published).
16. H. R. Tsai, I. Usov, A. Diaz, A. Menzel, and M. Guizar-Sicairos, "X-ray ptychography with extended depth of field," Opt. Express **24**(25), 29089–29108 (2016).
17. H. Simons, S. R. Ahl, H. F. Poulsen, and C. Detlefs, "Simulating and optimizing compound refractive lens-based X-ray microscopes," J. Synchrotron Radiat. **24**(2), 392–401 (2017).
18. H. M. L. Faulkner and J. M. Rodenburg, "Movable aperture lensless transmission microscopy: a novel phase retrieval algorithm," Phys. Rev. Lett. **93**(2), 023903 (2004).
19. P. Thibault, M. Dierolf, O. Bunk, A. Menzel, and F. Pfeiffer, "Probe retrieval in ptychographic coherent diffractive imaging," Ultramicroscopy **109**(4), 338–343 (2009).
20. F. Pfeiffer, "X-ray ptychography," Nat. Photonics **12**(1), 9–17 (2018).
21. F. Mastropietro, P. Godard, M. Burghammer, C. Chevallard, J. Daillant, J. Duboisset, M. Allain, P. Guenoun, J. Nouet, and V. Chamard, "Revealing crystalline domains in a mollusc shell single-crystalline prism," Nat. Mater. **16**(9), 946–952 (2017).
22. S. O. Hruszkewycz, M. Allain, M. V. Holt, C. E. Murray, J. R. Holt, P. H. Fuoss, and V. Chamard, "High-resolution three-dimensional structural microscopy by single-angle Bragg ptychography," Nat. Mater. **16**(2), 244–251 (2017).
23. H. Simons, A. C. Jakobsen, S. R. Ahl, C. Detlefs, and H. F. Poulsen, "Multiscale 3D characterization with dark-field x-ray microscopy," MRS Bull. **41**(6), 454–459 (2016).
24. A. Snigirev, V. Kohn, I. Snigireva, and B. Lengeler, "A compound refractive lens for focusing high-energy X-rays," Nature **384**(6604), 49–51 (1996).
25. A. F. Pedersen, H. Simons, C. Detlefs, and H. F. Poulsen, "The fractional Fourier transform as a simulation tool for lens-based X-ray microscopy," J. Synchrotron Radiat. **25**(3), 717–728 (2018).
26. A. F. Pedersen, *Andersfp/XFrFT: XFrFT* (Zenodo, 2017).
27. F. Seiboth, A. Schropp, M. Scholz, F. Wittwer, C. Rödel, M. Wünsche, T. Ullsperger, S. Nolte, J. Rahomäki, K. Parfeniukas, S. Giakoumidis, U. Vogt, U. Wagner, C. Rau, U. Boesenberg, J. Garrevoet, G. Falkenberg, E. C. Galtier, H. J. Lee, B. Nagler, and C. G. Schroer, "Perfect X-ray focusing via fitting corrective glasses to aberrated optics," Nat. Commun. **8**(1), 14623 (2017).
28. K. T. Murray, A. F. Pedersen, I. Mohashi, C. Detlefs, A. J. Morgan, M. Prasciolu, C. Yildirim, H. Simons, A. C. Jakobsen, H. N. Chapman, H. F. Poulsen, and S. Bajt, "Multilayer Laue lenses at high x-ray energies: Performance and applications," Opt. Express **27**(5), 7120 (2019).

Optics EXPRESS

29. A. Baroni, M. Allain, P. Li, V. Chamard, and P. Ferrand, "Joint estimation of object and probes in vectorial ptychography," Opt. Express **27**(6), 8143–8152 (2019).
30. A. J. Morgan, M. Prasciolu, A. Andrejczuk, J. Krzywinski, A. Meents, D. Pennicard, H. Graafsma, A. Barty, R. J. Bean, M. Barthelmess, D. Oberthuer, O. Yefanov, A. Aquila, H. N. Chapman, and S. Bajt, "High numerical aperture multilayer Laue lenses," Sci. Rep. **5**(1), 9892 (2015).
31. M. Prasciolu, A. F. G. Leontowich, J. Krzywinski, A. Andrejczuk, H. N. Chapman, and S. Bajt, "Fabrication of wedged multilayer Laue lenses," Opt. Mater. Express **5**(4), 748–755 (2015).
32. A. Andrejczuk, J. Krzywinski, and S. Bajt, "Influence of imperfections in a wedged multilayer Laue lens for the focusing of X-rays investigated by beam propagation method," Nucl. Instrum. Methods Phys. Res., Sect. B **364**, 60–64 (2015).
33. S. A. Alexandrov, T. R. Hillman, T. Gutzler, and D. D. Sampson, "Synthetic Aperture Fourier Holographic Optical Microscopy," Phys. Rev. Lett. **97**(16), 168102 (2006).
34. P. Godard, M. Allain, and V. Chamard, "Imaging of highly inhomogeneous strain field in nanocrystals using x-ray Bragg ptychography: A numerical study," Phys. Rev. B **84**(14), 144109 (2011).
35. H. F. Poulsen, P. K. Cook, H. Leemreize, A. F. Pedersen, C. Yildirim, M. Kutsal, A. C. Jakobsen, J. X. Trujillo, J. Ormstrup, and C. Detlefs, "Reciprocal space mapping and strain scanning using X-ray diffraction microscopy," J. Appl. Crystallogr. **51**(5), 1428–1436 (2018).